

Dispersion processes in weakly dissipative estuaries: Part 2. Multiple constituent tides.

Annalisa De Leo¹, Nicoletta Tambroni¹, and Alessandro Stocchino²

¹University of Genoa

²The Hong Kong Polytechnic University

November 22, 2022

Abstract

In the present study, we extend the analysis of the dispersion processes induced by tidal flow in weakly-dissipative estuaries discussed in the companion paper. Here we focus the attention on the flow induced by more realistic tidal waves provided by different combinations of semi-diurnal and diurnal constituents. We employ a large-scale physical model of a system composed by a large basin (open sea) and a compound tidal channel, where tides are produced as volume waves with prescribed shapes. Two-dimensional superficial velocity fields are used to study the main Eulerian and Lagrangian properties of the flow, in terms of absolute and relative particle statistics. The results suggest that the mixed character of the tides strongly influences the shape of the macro-vortices generated at the tidal inlet, whereas the overall residual currents seem to be less sensitive. Moreover, for the present tidal setting, longitudinal dispersion, the dominant dispersion process, is enhanced when the semi-diurnal constituents prevail. Finally, multiple particle statistics show regimes typical of non-local dynamics for particle separation larger than a typical injection length scale, which is the size of the tidal inlet. Non-local dynamics imply that the dispersion is dominated by flow structures larger than the mean separation length, i.e. the tidal wavelength and the size of the macro-vortices. The present results together with those discussed in Part 1, offer a thorough insight in the main dispersion processes induced by tidal flows, which are extremely relevant in the case of estuarine dynamics.

1 **Dispersion processes in weakly dissipative estuaries:**
2 **Part 2. Multiple constituent tides.**

3 **A. De Leo¹, N. Tambroni¹, and A. Stocchino²**

4 ¹Dipartimento di Ingegneria Civile, Chimica e Ambientale, Università degli Studi di Genova, via
5 Montallegro 1, 16145, Genova, Italia

6 ²Department of Civil and Environmental Engineering, Hong Kong Polytechnic University, Hung Hom,
7 Kowloon, Hong Kong

8 **Key Points:**

- 9 • The harmonic content of the tidal waves controls the generation of macro-vortices
10 at the tidal inlet inducing vortices at different scales
11 • For the present tidal setting, longitudinal dispersion is enhanced in mixed tides
12 with semi-diurnal constituent dominance
13 • Dispersion processes are dominated by non-local dynamics for particle separations
14 larger than the typical injection scale.

Corresponding author: Annalisa De Leo, annalisa.deleo@edu.unige.it

Abstract

In the present study, we extend the analysis of the dispersion processes induced by tidal flow in weakly-dissipative estuaries discussed in the companion paper. Here we focus the attention on the flow induced by more realistic tidal waves provided by different combinations of semi-diurnal and diurnal constituents. We employ a large-scale physical model of a system composed by a large basin (open sea) and a compound tidal channel, where tides are produced as volume waves with prescribed shapes. Two-dimensional superficial velocity fields are used to study the main Eulerian and Lagrangian properties of the flow, in terms of absolute and relative particle statistics. The results suggest that the mixed character of the tides strongly influences the shape of the macro-vortices generated at the tidal inlet, whereas the overall residual currents seem to be less sensitive. Moreover, for the present tidal setting, longitudinal dispersion, the dominant dispersion process, is enhanced when the semi-diurnal constituents prevail. Finally, multiple particle statistics show regimes typical of non-local dynamics for particle separation larger than a typical injection length scale, which is the size of the tidal inlet. Non-local dynamics imply that the dispersion is dominated by flow structures larger than the mean separation length, i.e. the tidal wavelength and the size of the macro-vortices. The present results together with those discussed in Part 1, offer a thorough insight in the main dispersion processes induced by tidal flows, which are extremely relevant in the case of estuarine dynamics.

Plain Language Summary

Tides are generated by combined astronomical forces among Earth, Moon and Sun. Unbalance between gravitational attraction and centrifugal force is the driving mechanism for ocean tides. Interestingly tides are composed by several constituents that can be mainly grouped in semi-diurnal (lunar and solar) and diurnal (lunar and solar) constituents. The presence of several harmonics dramatically influences the shape of the astronomical tide, whose form also changes during its propagation in shallow confined regions like coastal areas and estuaries. Here we are interested to understand how the shape of the tidal wave can influence the dispersion processes that occur in real estuaries. To this end we employ a large-scale laboratory model of an estuary and consider the flow generated by different tidal forcings, composed by semi-diurnal and diurnal constituents with varying phase lag and relative amplitude. Free surface velocity measurements are used to evaluate the main features of the transport processes, mainly related to longitudinal dispersion. Our results suggest that the mixed character of the tides may play an important role on the dispersion processes, enhancing the ability of the flow to transport mass in the main flow direction.

1 Introduction

Estuaries are considered transitional regions between landward waters and open sea, and thus important sites for human development. Estuarine regions can be classified depending on morphology, geometry configurations, vertical salinity stratification and finally hydrodynamics (Valle-Levinson, 2010). In particular, coastal bays and estuaries are characterized by flows mainly owed to hydraulic unbalance such as baroclinic pressure gradients, river inflows and wind stresses. If on one hand, tidal propagation has been deeply studied in order to better understand the suitable parameter to describe it (Seminara et al., 2010; Toffolon et al., 2006; Cai et al., 2012), on the contrary, less is known about the role of tidal circulation on transport processes. Tides are long-period waves induced by gravitational force unbalanced among Earth, Moon and Sun. In particular, astronomical tides are composed by several tide constituents, with different amplitude and periods, yielding to complex tidal waves (Lee & Chang, 2019). Moreover, daily and seasonal variations might occur depending on the combination of the main constituents.

65 Several studies focus on the definition of the time scales and the estimation of the dis-
 66 persion coefficients in monochromatic tidal force conditions (see Cucco et al., 2009; Umgiesser
 67 et al., 2014; Viero & Defina, 2016, among others). At the same time, several studies have
 68 been dedicated to the prediction of multi-harmonic tides (Amin, 1986; Lee & Chang, 2019)
 69 and their propagation (Jay, 1991; Seminara et al., 2010; Fortunato & Oliveira, 2005; Tof-
 70 folon et al., 2006; Cai et al., 2012). However, the investigation of the effects of multiple
 71 harmonics on the flow field and dispersion processes lacks of evidence. In fact, field stud-
 72 ies devoted to the estimate of longitudinal dispersion coefficients (Monismith et al., 2002;
 73 Lewis & Uncles, 2003; Banas et al., 2004) did not provide a relationship among the co-
 74 efficients and the tide wave shape. In the companion paper, Part 1, we focused our at-
 75 tention on the description of the flow field generated by a single harmonic tide on a large
 76 scale physical model of a basin, representing the open ocean, connected to a compound
 77 tidal channel through an inlet entrance. The aim was to asses a detailed Lagrangian de-
 78 scription of the typical integral scales and single particle statistics, varying the control-
 79 ling parameters in a simplified tidal forcing range. Dispersion coefficients have been eval-
 80 uated and discussed as a function of the main external parameters following Toffolon et
 81 al. (2006). Employing the same experimental set up and the same Large Scale Particle
 82 Image Velocimetry technique, this second part of the work is devoted to extend the La-
 83 grangian analysis to a more realistic context, i.e. tides composed by the contemporary
 84 coexistence of semi-diurnal and diurnal constituents. The flow structures are expected
 85 to be more complicated by the presence of multiple harmonics with possible effects on
 86 the main dispersion processes (Zimmerman, 1986). To assess the interplay of flow struc-
 87 tures at different scales and the resulting dispersion regimes, multiple particle statistics
 88 have proven to be an effective analysis when applied to geophysical flows (LaCasce, 2008).
 89 In fact, the theoretical results in terms of relative dispersion and Finite Size Lyapunov
 90 Exponents suggest the possible existence of local and non-local dynamical behaviors (Kraichnan,
 91 1966; Lin, 1972; Bennett, 1984; Babiano et al., 1990). The latter regimes are associated
 92 to particle separations that are influenced by different flow scales. Applications to geo-
 93 physical flows showed the existence of both regimes when the flow is mainly generated
 94 by the tides (Enrile et al., 2019). In the present study, we will perform multiple parti-
 95 cles statistics based on the measured flow fields of both the single harmonic case as well
 96 in the case of multiple harmonics tides.

97 The paper starts with a brief description of the experimental apparatus, already
 98 discussed in detail in Part 1; a characterization of the tidal forcing employed follows. In
 99 Section 3, we asses the governing parameters and describe the tidal propagation that oc-
 100 curs within the physical model. Eulerian and Lagrangian analysis follows describing in
 101 details the flow characteristics, identifying vortical structures using the Okubo-Weiss pa-
 102 rameter (Okubo, 1970) and evaluating the influence of the initial conditions on the La-
 103 grangian scales. A comparison of the multiple particle statistics and Finite-Size Lyapunov
 104 Exponent (FSLE) between Part 1 and Part 2 is then provided.

105 **2 Experimental Methods**

106 **2.1 Laboratory set-up and measuring technique**

107 We employ the same experimental apparatus and measuring techniques adopted
 108 for the single-component tide experiments described in the companion paper, Part 1. Here
 109 we briefly recall the main features of the laboratory apparatus. Our main goal is to mea-
 110 sure two dimensional velocity fields on the free surface layer induced by a controlled tidal
 111 oscillation in a large scale shallow flume. The flume is approximately 29 m long and 2.42
 112 m wide. At one end a cylinder is free to oscillate in a feeding tank according to a pre-
 113 scribed time law in order to produce a tidal wave. The latter then propagates in a 6 m
 114 long rectangular channel before crossing a tidal inlet at the beginning of a 23 m com-
 115 pound channel. The channel cross section is composed by a 0.24 m deep main channel
 116 and two lateral tidal flats. Moreover, the main channel has a longitudinal slope of about

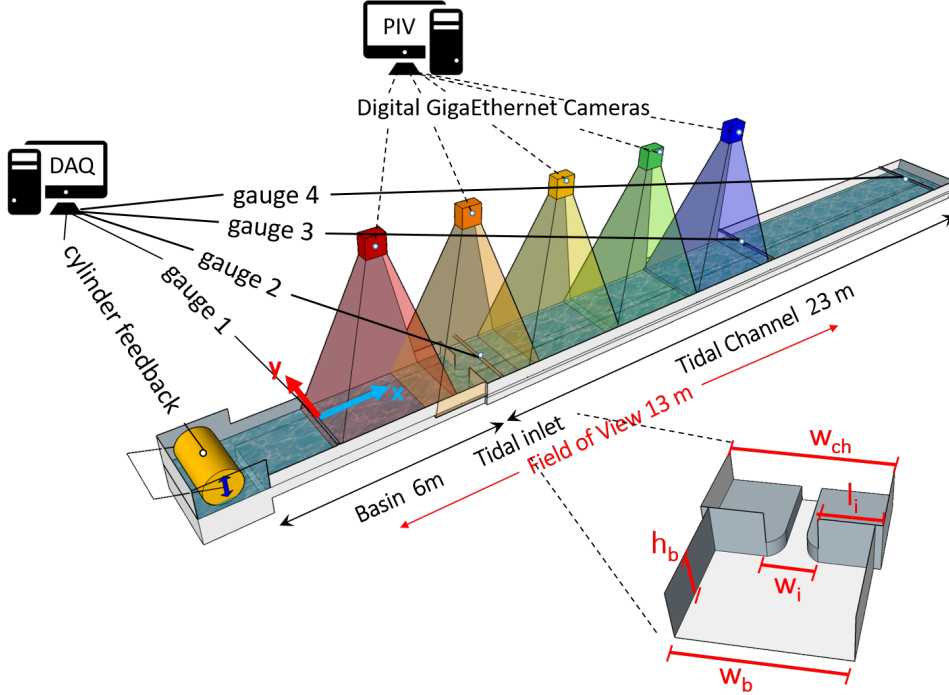


Figure 1. Sketch of the experimental set up and measuring systems.

117 2.5‰ and an exponentially landward decreasing width (w_i), varying from about 70 cm
 118 at the tidal inlet to about 11 cm at its closed end. Consequently, the tidal flats width
 119 ranges between 0.86 m and 1.16 m on each side. Figure 1 shows a sketch of the exper-
 120 imental flume and setup. Two dimensional superficial velocity fields $\mathbf{u}(\mathbf{x}, t) = (u(\mathbf{x}, t), v(\mathbf{x}, t))$
 121 have been measured using a Particle Image Velocimetry equipment specifically designed
 122 for the present purpose to obtain a large field of measurements, approximately $13 \text{ m} \times$
 123 3 m . The image acquisition system is composed by five digital cameras (Teledyne Dalsa
 124 Genie Nano 4 of model C1280 and 1 of model C2450). The system allowed us to record
 125 at a frequency of 10 Hz. The images, obtained after a pre-processing providing a single
 126 image for each instant, have been analysed using the software proVision-XSTM (Inte-
 127 grated Design Tools Inc). Finally, free surface elevation has been monitored at four con-
 128 trol points along the entire channel using ultrasound gauges (Honeywell model 946-A4V-
 129 2D-2C0-380E, with 30 cm range and an accuracy of 0.2% of the full scale). More details
 130 are provided in the companion paper.

131

2.2 Multiple constituents tidal forcing generation

Differently from the experiments described in the Part 1, here we have considered a more complex tidal forcing composed of different harmonics. Astronomical tide is indeed provided by a wide variety of harmonic constituents each one associated to a different gravitational force interaction between Earth, Moon and Sun. In terms of amplitude, the first four main tidal contributions are: the principal lunar semi-diurnal (M_2 , 12.42 hr period), the principal lunar diurnal (K_1 , 23.93 hr), the principal solar semi-diurnal (S_2 , 12 hr period), and the principal solar diurnal (O_1 , 25.82 hr). Grouping together the diurnal and semidiurnal components a simplified form for the astronomical tidal free sur-

Table 1. Experimental forcing tide parameters

	exp	T_{sd} [s]	T_d [s]	a_{sd} [m]	a_d [m]	ϕ [m]	F
	001	100	200	0.0042	0.00016	0	0.04
series 1	002	100	200	0.003	0.0006	0	0.20
	003	100	200	0.003	0.0009	0	0.30
	004	100	200	0.003	0.0013	0	0.44
	005	100	200	0.0022	0.00185	0	0.84
	006	100	200	0.0018	0.0022	0	1.20
	007	100	200	0.0014	0.0025	0	1.69
	series 2	008	100	200	0.003	0.0006	$-\pi/4$
009		100	200	0.003	0.0009	$-\pi/4$	0.30
010		100	200	0.003	0.0013	$-\pi/4$	0.44
011		100	200	0.0022	0.00185	$-\pi/4$	0.84
012		100	200	0.0018	0.0022	$-\pi/4$	1.20
013		100	200	0.0014	0.0025	$-\pi/4$	1.69
series 3	014	100	200	0.003	0.0006	$\pi/4$	0.20
	015	100	200	0.003	0.0009	$\pi/4$	0.30
	016	100	200	0.003	0.0013	$\pi/4$	0.44
	017	100	200	0.0022	0.00185	$\pi/4$	0.84
	018	100	200	0.0018	0.0022	$\pi/4$	1.20
	019	100	200	0.0014	0.0025	$\pi/4$	1.69

face oscillation reads:

$$\eta(t) = (A_{M2} + A_{S2}) \sin(\omega t) + (A_{K1} + A_{O1}) \sin\left(\frac{\omega}{2}t + \phi\right) = a_{sd} \sin(\omega t) + a_d \sin\left(\frac{\omega}{2}t + \phi\right) \quad (1)$$

where η is the free surface elevation, ω is the tidal angular frequency related to the semi-diurnal tidal period $T=12$ hr and ϕ is the phase shift. The reasons that induce us to use a simplified form will be explained later on. The relative importance of the semi-diurnal and diurnal components can be expressed through the form factor F defined as (Lee & Chang, 2019):

$$F = \frac{A_{K1} + A_{O1}}{A_{M2} + A_{S2}} = \frac{a_d}{a_{sd}} \quad (2)$$

132 The form parameter can be used to discriminate the different types of astronomical tide,
133 in particular:

- 134 • if $F < 0.25$, the tide is semi-diurnal;
- 135 • if $0.25 < F < 1.25$, the tide is mixed, but mainly semi-diurnal;
- 136 • if $1.25 < F < 3.0$, the tide is mixed, but mainly diurnal;
- 137 • if $F > 3.0$, the tide is diurnal.

138 According to Tsimplis et al. (1995) the form parameter associated with the astro-
139 nomical tide observed in different places in the Mediterranean Sea spans over a wide range
140 of values. As shown in Table 1, in our experiments we have thus considered different tidal
141 forcings with form parameter varying between 0.038 and 1.7. Note that in our labora-
142 tory model we have investigated the role of diurnal and semidiurnal tides by imposing
143 free surface oscillations according to (1). Hence, only two tidal periods have been set,
144 one for the semi-diurnal constituents (T_{sd}) and one for the diurnal constituents ($2T_{sd}$),
145 which are exactly multiple of each other. We acknowledge that observed semi-diurnal
146 (M_2 , S_2) and diurnal (K_1 , O_1) are characterized by different periods and this difference

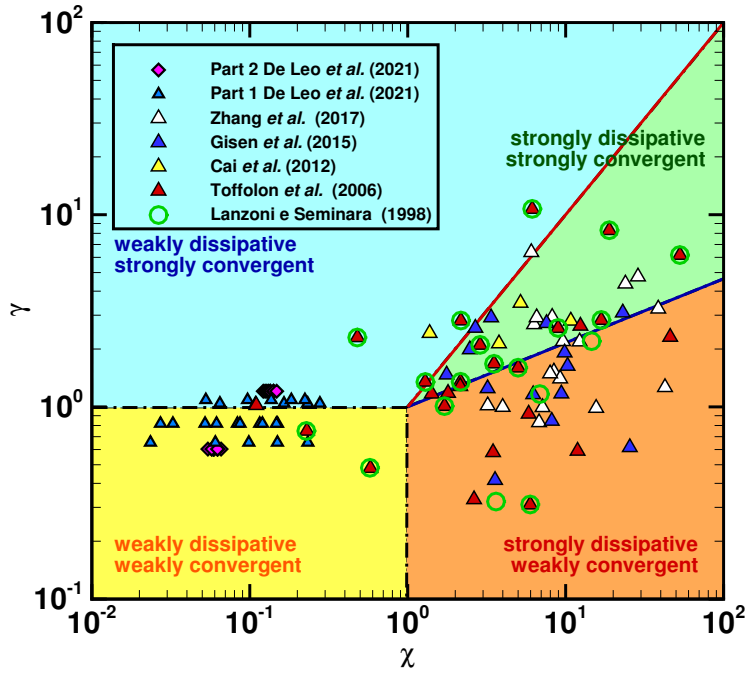


Figure 2. (χ, γ) -plane classification of the present experiments, experiments of Part 1 and of field observations as reported in Lanzoni and Seminara (1998), Toffolon et al. (2006), Cai et al. (2012) Gisen and Savenije (2015) and (Zhang & Savenije, 2017). $\gamma = \chi$ boundary (thick red line) and the $\gamma = \chi^{1/3}$ law (thick blue solid line) are also reported.

147 in periods leads to mixed tidal patterns with weekly variations (spring tide - neap tide
 148 cycles). However, reproducing this process at laboratory scales would have implied the
 149 acquisition of an unmanageable number of images, since our statistics are based on the
 150 average of several periods of the slowest modulation. Moreover, the phase shift introduced
 151 in equation (1) has been varied to understand the role of the tidal wave shape depend-
 152 ing of the phase lag between the semi-diurnal and diurnal constituents. Three series of
 153 experiments have been performed for a total of 19 experiments varying the form factor
 154 F and the phase ϕ , see Table 1 for the relevant experimental parameters. In particular,
 155 a first series of experiments (experiments from 2 to 7) has been designed for different val-
 156 ues of the form factor and vanishing phase. A second series (from experiment 8 to 13)
 157 has been performed for the same form factor of the first series, but choosing $\phi = -\pi/4$.
 158 The phase shifts has been changed to $\phi = \pi/4$ in the final series (from experiment 14
 159 to 19) of experiments. Note that the limiting cases of strongly semi-diurnal tides (ex-
 160 periment 1, for instance) or strongly diurnal tides ($F > 1.7$) have been extensively dis-
 161 cussed in the companion paper, referring to the single harmonic case.

162 3 Governing parameters and tidal propagation

163 In this section, we describe the external parameters that have been used to differen-
 164 tiate the experiments. The first non dimensional parameter that will be used is the
 165 form factor F , see equation 2, as introduced by Lee and Chang (2019), describing the
 166 semi-diurnal or diurnal dominance. However, the introduction of multiple constituents
 167 as analytically represented by equation (1) is characterized by the presence of two differ-

ent tidal periods, thus raising problems when one typical time scale must be selected. Indeed, the use of the external parameters introduced in Part 1 for the monochromatic tide experiments is here complicate. Let us recall that in the compainon paper, following Toffolon et al. (2006), we have considered as external parameters the convergence ratio γ , and the friction parameter χ , defined as the ratio between frictional forces and inertial forces. They read:

$$\gamma = \frac{L_g}{2\pi L_b}, \quad \chi = \epsilon \frac{L_g}{2\pi C^2 R_h}, \quad \text{with} \quad L_g = T\sqrt{gR_h}, \quad (3)$$

where $\epsilon = a/R_h$ is the non dimensional tidal amplitude, R_h is the hydraulic radius, L_b the convergence length and T the tidal period. Thus, they require the identification of a typical relative tidal amplitude ϵ and a tidal period T . The choice for the latter scales is straightforward when a monochromatic tide is considered, whereas in the simultaneous presence of more than one constituent it requires care. Note that Toffolon et al. (2006) and later Cai et al. (2012) applied their models to realistic estuaries where tides are formed by lunar and solar constituents with different periods, but dominated by the semi-diurnal lunar tide M_2 . In the present study, we set the non dimensional tidal amplitude as the ratio between half the tidal excursion, defined as the difference between the highest and lowest water level and the hydraulic radius. We recall that all the three series of experiments have been designed in order to maintain the same tidal range, whilst varying the form factor and the phase shift. As far as the typical tidal period is concerned, we select the dominant period as the one of the higher amplitude constituent. Thus, the friction parameter χ has been calculated the latter. The values of the three series of experiments have been reported in the $(\gamma; \chi)$ -plane plot shown in Figure 2 together with the experiments discussed in Part 1 and several field observations (Lanzoni & Seminara, 1998; Toffolon et al., 2006; Cai et al., 2012; Gisen & Savenije, 2015; Zhang & Savenije, 2017). As expected, the values of the χ parameter of all the present experiments are grouped around two values, since the amplitude is the same except for an obvious small experimental variation and the dominant tidal periods are two. Similarly to experiments of Part 1, our experimental model is representative of a weakly convergent-weakly dissipative estuary as described by Toffolon et al. (2006). It is now interesting to observe how the imposed tidal signals with different shapes (different form factor F) propagate from the flume basin (open sea condition) through the tidal inlet and along the compound channel. It is well known that nonlinearity is able to amplify the tidal wave amplitude and to produce higher harmonics, even with simple tidal wave forms (Lanzoni & Seminara, 1998; Toffolon et al., 2006). The theoretical model by Toffolon et al. (2006) showed how the marginal conditions for tidal wave amplification in estuaries may be strongly affected by the amplitude of tidal wave depending on the external parameters γ and χ . The marginal conditions have been provided as $\gamma = k\chi^m$, where the coefficients k and m strongly depend on the relative tidal amplitude. For the parameters γ and χ , and the relative amplitude ϵ of the present experiments, the theoretical model by Toffolon et al. (2006) predicts amplification of the tidal waves. Three examples of tidal propagation are shown in Figure 3. In particular, they refer to experiment 2 ($F = 0.2$ semi-diurnal tide), experiment 4 ($F = 0.444$, mixed tide mainly semi-diurnal) and experiment 7 ($F = 1.686$, mixed tide mainly diurnal). Panels a), b) and c) report water level measurements in the middle of three channel cross sections (see Figure 1 for the gauge positions) along the flume; the corresponding FFT analysis is plotted in panels d), e) and f). As expected tidal amplification is observed in all the cases leading to amplitudes in the tidal channel far from the inlet, even three times higher than at the flume basin (forcing wave). Note that in general, in agreement with the linear theory predictions for weakly convergent and weakly dissipative estuaries, both the diurnal and semidiurnal components amplify. However, the semidiurnal component is subject to a larger amplification than the diurnal one, this is related both to non-linearities and also to the occurrence that the mode associated to the semidiurnal component is closer to the resonant mode of our experimental model than the one associated to the diurnal component.

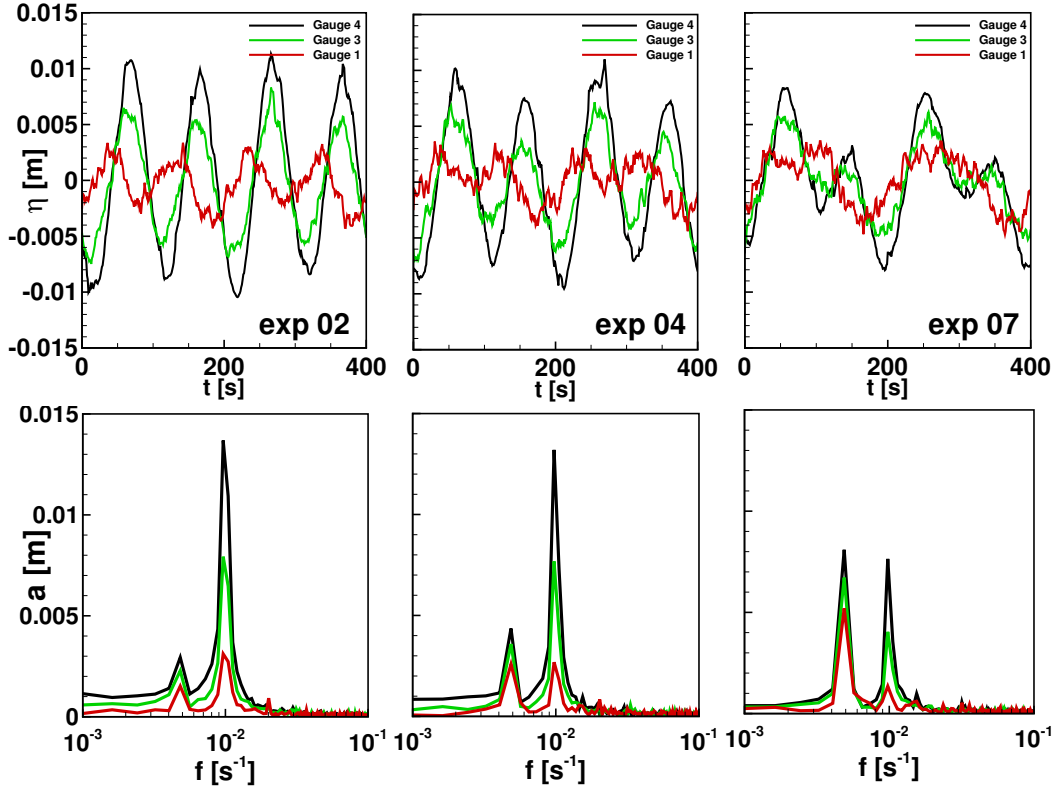


Figure 3. Example of tidal propagation from the flume basin (gauge 1, open sea condition) along the tidal channel (gauge 3 and 4 placed at 14.5 m and 25 m, respectively, from gauge 1) for experiment 2 ($F = 0.2$ semi-diurnal tide), experiment 4 ($F = 0.444$, mixed tide mainly semi-diurnal) and experiment 7 ($F = 1.686$, mixed tide mainly diurnal). Bottom panel, corresponding FFT analysis of the water level signals. The same colors are used for the gauge signals and their corresponding FFT.

4 The effect of multiple tidal harmonics on the time dependent flow and the generation of a residual current

In this section, we discuss the role of the tidal wave shape on the time dependent two dimensional velocity fields $\mathbf{u}(\mathbf{x}, t) = (u(\mathbf{x}, t), v(\mathbf{x}, t))$ measured using the PIV technique. Vortical structures have been identified using the Okubo-Weiss parameter λ_0 (Okubo, 1970; Weiss, 1991), defined as $\lambda_0 = 1/4(S^2 - \omega^2)$, where $S^2 = S_n^2 + S_s^2$ is the total square strain, sum of the normal (S_n) and shear (S_s) components, and ω^2 is the square of the vorticity. Positive values of λ_0 indicate flow regions dominated by shear, whereas negative values of λ_0 indicate the presence of vortices. Here, we are mostly interested to understand how the relative importance of the semi-diurnal and diurnal constituents might influence the generation of flood macro-vortices at the tidal inlet. The generation mechanisms of flood vortices have been subject to several studies in the last years (Wells & van Heijst, 2004; Nicolau del Roure et al., 2009; Vouriot et al., 2019). The driving mechanism has been described in terms of vortex shedding at the corners of the tidal inlet. The generation of flood vortices is only slightly influenced by the shape of the inlet itself (Nicolau del Roure et al., 2009). In the present case, the tidal inlet of the laboratory flume can be classified as a *barrier island* as described in Nicolau del Roure et al. (2009), where the inlet is centered with the tidal channel and the lateral obstructions are thin compared to their length. During the flood phase the flow is forced to enter the

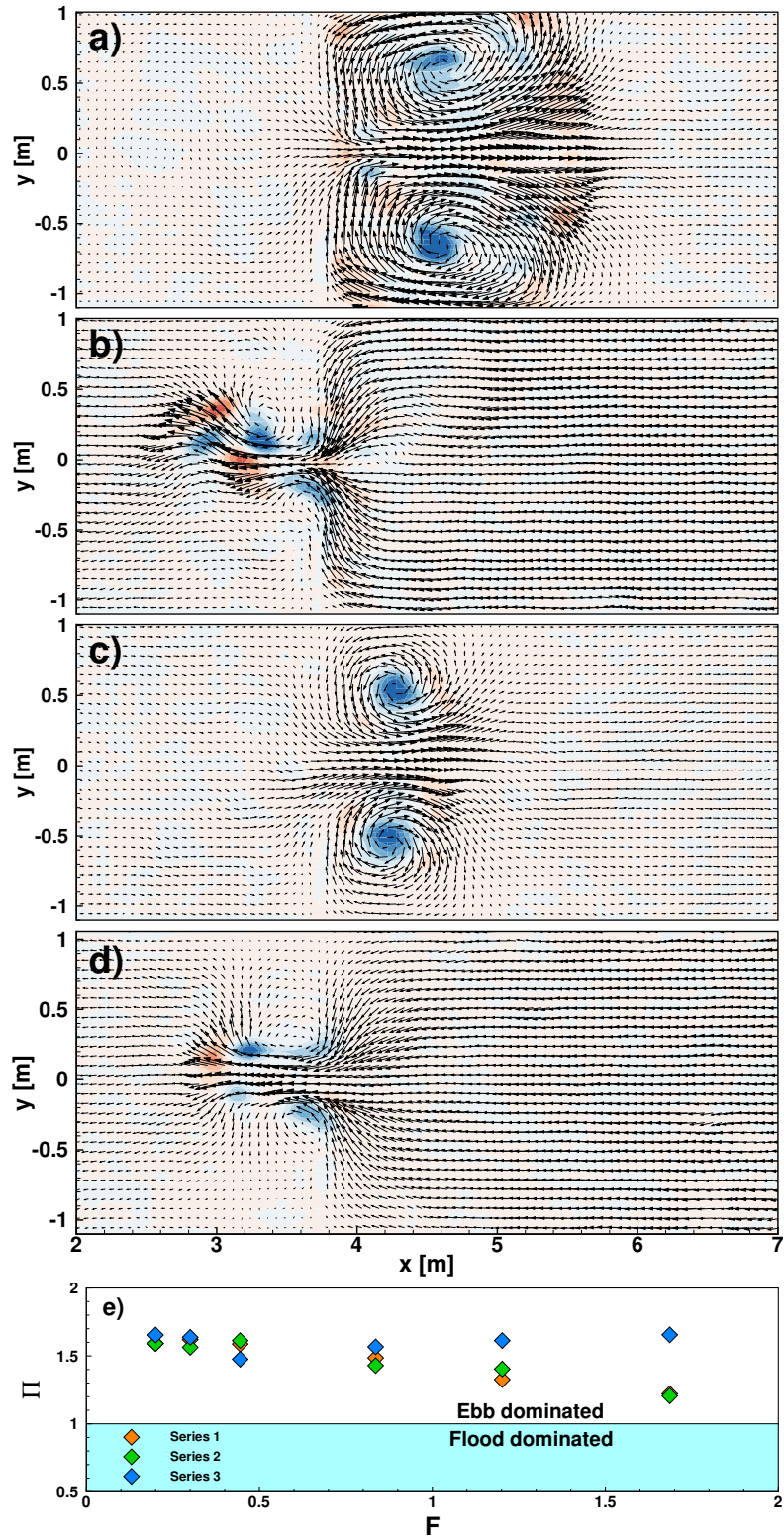


Figure 4. Examples of time dependent two dimensional velocity fields with Okubo-Weiss parameter contours for experiment 5. Panel a) maximum crest flood phase; panel b) and d) flushing ebb phase; panel c) less intense flood. Panel e) Power ratio of ebb and flood powers computed as the time integral of the kinetic energy per unit mass as a function of the form factor F

240 tidal channel through the inlet and the interaction with the sharp corners generates vor-
 241 ticity that is then stretched and convected towards the channel. The vortex shedding
 242 is regulated by the non dimensional frequency described by the Strouhal number $S_t =$
 243 L/UT , where L is a typical length scale related to the vortex shedding generation, U
 244 is a convective velocity scale and T is the typical tidal period. In this case, the typical tidal
 245 period could be considered the period of the dominant tidal constituents and, thus, de-
 246 pends on the form factor F . The flood-macro-vortices develop during each cycle and then
 247 are found to be flushed out or to remain in the channel depending the values of the Strouhal
 248 number (Wells & van Heijst, 2004). A critical Strouhal number has been suggested by
 249 Wells and van Heijst (2004) and takes the value of 0.13. For values lower than the crit-
 250 ical one, the macro-vortices are expected to be completely flushed out, whereas they do
 251 not completely decay and remain confined in the channel close to the inlet for Strouhal
 252 greater than 0.13. It is worth noting that the theoretical model of Wells and van Hei-
 253 jst (2004), later confirmed by several Authors (Nicolau del Roure et al., 2009; Vouriot
 254 et al., 2019), has been developed for a monochromatic tide in a basin with constant depth.
 255 On the contrary, the experimental observations discussed in the companion paper, Part
 256 1, show that the presence of lateral tidal flats are responsible to flush out the flood-vortices
 257 regardless the value of the Strouhal number, as reported in other studies with tidal com-
 258 pound channels (Kang & Jun, 2003; Fortunato & Oliveira, 2005). Tidal flats typically
 259 induce ebb dominance and this is the main reason for the apparent discrepancy with the
 260 cited theoretical and laboratory studies. In the present case, the generation and evolu-
 261 tion of the flood-macro-vortices is further complicated by a multiple-constituents forc-
 262 ing with different shapes and phase lags of the two harmonics. For very low and high
 263 values of the form parameter F , the tides are mainly semi-diurnal and diurnal, i.e. dom-
 264 inated by a single harmonic. In these cases the flood-macro-vortices behave in the same
 265 way as described in Part 1. More interestingly, in the cases of mixed tides, i.e. for $0.25 <$
 266 $F < 3$, the tidal waves show intermediate crests and troughs. Typical examples of time
 267 dependent two dimensional velocity fields with superimposed contours of the Okubo-Weiss
 268 parameter λ_0 are shown in Figure 4 panel a) - d), for experiment 5 with $F = 0.836$ and
 269 $\phi = 0$. In particular, two different classes of flood-macro-vortices are generated depend-
 270 ing on the tidal wave crests. In fact, a larger size macrovortices is formed in the flood
 271 phase corresponding to the maximum crest, see panel a). The size of the latter struc-
 272 ture is comparable to the macrovortices generated in the case of the single harmonic forc-
 273 ing with the same period and relative amplitude. The flood-macro-vortices are then flushed
 274 away during the ebb phase, see panel b). Secondary macrovortices, the size of which is
 275 significantly smaller, typically around half of the primary macrovortices (see panel c)),
 276 are generated in correspondence of the second, less intense, tidal crest. Also these sec-
 277 ond macrovortices are flushed away during the ebb phase. The generation of both pri-
 278 mary and secondary vortices is associated to a mechanism of vortex shedding and vor-
 279 tex merging, as already discussed in Part 1. In the supplementary material we provide
 280 a movie showing the vortex merging mechanism for the cases of mixed tides, experiment
 281 5. Finite size vortices emitted by the corners of the barrier island are convected by the
 282 main flow and embedded in the main macro-structure, increasing its size. A deeper anal-
 283 ysis on the Strouhal numbers shows that for values of F lower than 0.6, the Strouhal is
 284 higher than the Wells and van Heijst (2004)'s critical value, whereas, for $F > 0.6$, it
 285 is lower than 0.13, but also in this case as for the experiments discussed in Part 1, the
 286 primary and secondary flood-macro-vortices are found to be flushed out towards the basin
 287 (open sea). This can be associated to the ebb dominant character of the flow field. In-
 288 deed, also for the present experiments, the power ratio $\Pi = P_{ebb}/P_{flood}$, where $P_{ebb}(P_{flood})$
 289 represent the power computed as the time integral of the kinetic energy per unit mass
 290 during the ebb (flood) phase, is found to be always greater than 1, see Figure 4 panel
 291 e). Interestingly, the power ratio tends to slightly decrease with the form factor F , ex-
 292 cept for the series 3 ($\phi = \pi/4$). The differences observed among the different series could
 293 be explained considering the tidal signals imposed in the three cases. For series 1 and
 294 2 the tidal prism, defined as the amount of water that enters and exits the channel in

295 a tidal cycle (Fagherazzi et al., 2013), calculated using the imposed water level η would
 296 suggest a tendency to have an almost vanishing tidal prism (series 1) and a flood dom-
 297 inated character (series 2). However, the presence of the tidal flats yields to a clear ebb
 298 dominance. In the case of series 3, the phase lag $\phi = \pi/4$ generates a stronger asym-
 299 metry between the ebb and flood phase, producing an increased ebb dominance of the
 300 flow.

301 A last comment concerns the effect of multiple-constituents on the residual currents
 302 generated by the periodic forcing. The importance of the residual currents on the net
 303 mass transport has been widely recognized, especially when considering the mixing pro-
 304 cesses associated to long time transport, i.e. over a time scale of numerous tidal cycles
 305 (Valle-Levinson, 2010). As in the companion paper, we have evaluated the steady ve-
 306 locity fields $\mathbf{U}(\mathbf{x}, t)$ by averaging over the total number of tidal cycles recorded during
 307 a single experiment. In the present case, however, the tidal wave assumes different shapes
 308 depending on the form factor and the possible phase lags. As discussed above, mixed tides
 309 generate primary and secondary flood-macro-vortices, the latter showing a much smaller
 310 typical size. The residual currents, generated by multiple tidal cycles, appear to be quite
 311 similar to the ones obtained in the case of monochromatic tides. Examples of residual
 312 velocity fields are shown in Figure 5 from panel a) to panel f) for all experiments of se-
 313 ries 1. The six shown experiments span the studied range of the form factor F . By in-
 314 specting Figure 5, it clearly appears that the shape of the residual currents does not sub-
 315 stantially change with F . Averaging over several cycles seems to filter out the secondary
 316 flood-macro-vortices leaving only the trace of the largest flood-macro-vortices. On the con-
 317 trary, as shown in panel g) of Figure 5, the intensity of the residual current relative to
 318 the tidal peak velocity ($|u_p|$) seems to decrease for increasing F both in terms of mean
 319 intensity (square symbols) and maximum residual velocities (diamonds symbols). This
 320 is in agreement with what observed in the case of monochromatic tides for increasing pe-
 321 riod and constant relative tidal amplitude. In fact, the diurnal component tends to dom-
 322 inate for increasing form factor and, for constant ϵ , this leads to weaker residual currents.
 323 We also observe also that, in the present experiments, the residual currents could reach
 324 intensities up to 50% of the peak tidal velocities. The fact that the time dependent ve-
 325 locity fields and the steady components (residuals) assume quite a different behavior could
 326 influence the mixing processes. In fact, we expect that the presence of secondary flood-
 327 macro-vortices in the case of strongly mixed tides could modify the Lagrangian proper-
 328 ties of the transport processes.

329 5 Lagrangian analysis and dispersion regimes

330 5.1 The influence of the initial conditions on the Lagrangian scale

331 Following the same approach of the analysis performed in Part 1 for the monochro-
 332 matic tidal wave, we base the evaluation of the main Lagrangian quantities on the com-
 333 putation of numerical trajectories starting from the two dimensional Eulerian velocity
 334 fields. In this section, we will discuss the normalized velocity autocorrelation functions
 335 \mathcal{R}_{uu} and \mathcal{R}_{vv} , defined as $\mathcal{R}_{uu}(\tau) = (\langle u(t)u(t+\tau) \rangle) / \mathcal{R}_{uu}(0)$ and $\mathcal{R}_{vv}(\tau) = (\langle v(t)v(t+\tau) \rangle) / \mathcal{R}_{vv}(0)$, where the brackets indicate an average over all particle trajectories and τ
 336 the time lag. The autocorrelations are then used to evaluate the Lagrangian integral scales
 337 T_u and T_v as $T_u = \int_0^{+\infty} \mathcal{R}_{uu} d\tau$ and $T_v = \int_0^{+\infty} \mathcal{R}_{vv} d\tau$ (Taylor, 1921). The Lagrangian
 338 integral scale of the process is finally computed as $T_L = 1/2(T_u + T_v)$ that represents
 339 the decorrelation time of the dispersion process, i.e. the time required to a tracer par-
 340 ticle to loose memory of its initial conditions (position and velocity) (Taylor, 1921; La-
 341 Casce, 2008). Differently from Part 1, tidal waves are more complex and their shapes
 342 have been varied in the three series of experiments. From an Eulerian point view, the
 343 more complex tidal forcing has proven to generate flow structures at different length scales
 344 that are periodically generated and destroyed, especially in the mixed tide cases. Since
 345 the dynamical processes appeared to be more complicate than in the monochromatic case,
 346

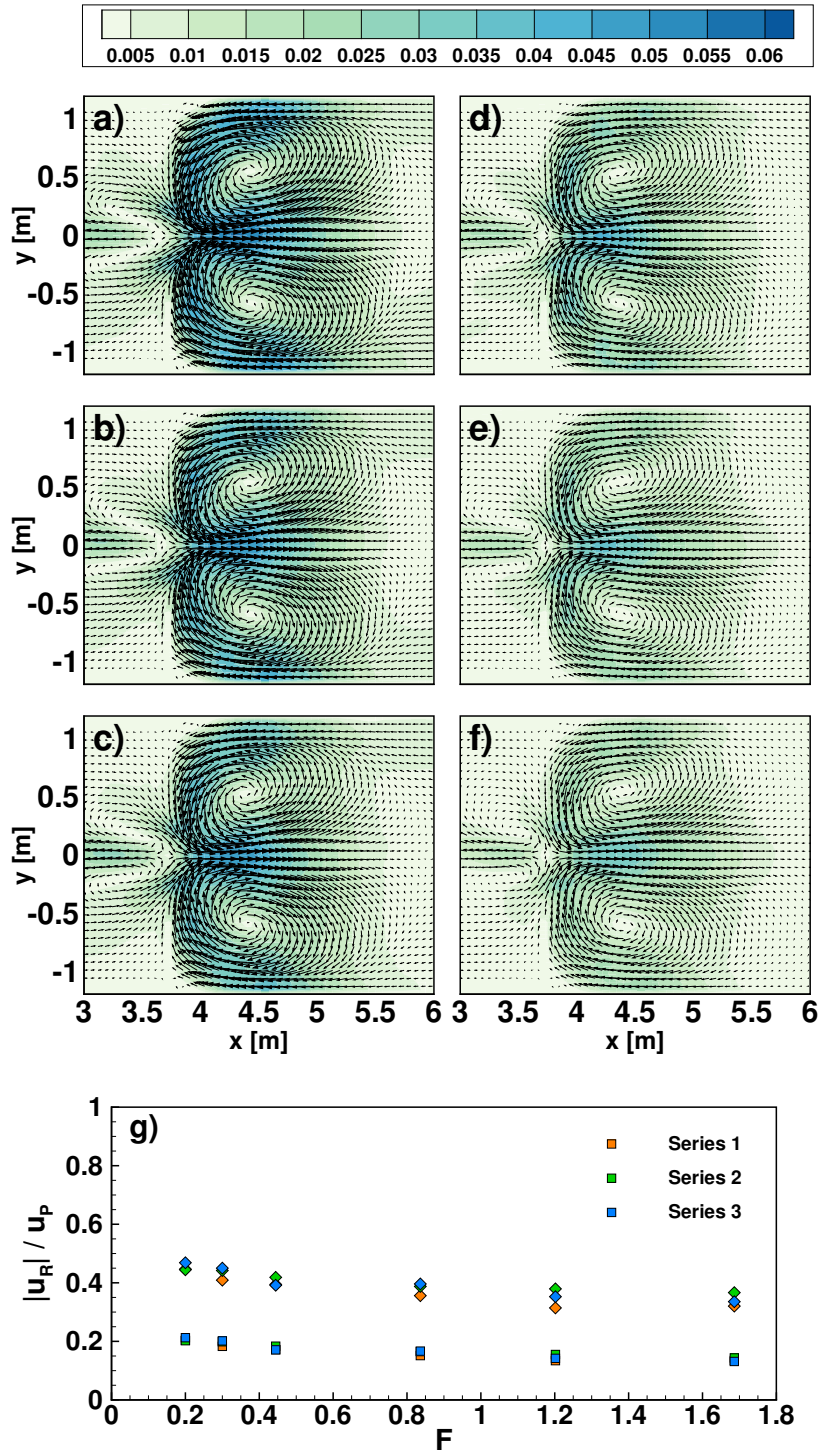


Figure 5. Panel a) to f): examples of residual currents fields for experiments of series 1. g): average residual velocity (squares) and maximum residual velocity (diamonds) divided by the tidal velocity peak at the inlet ($|u_p|$) as function of the form factor F .

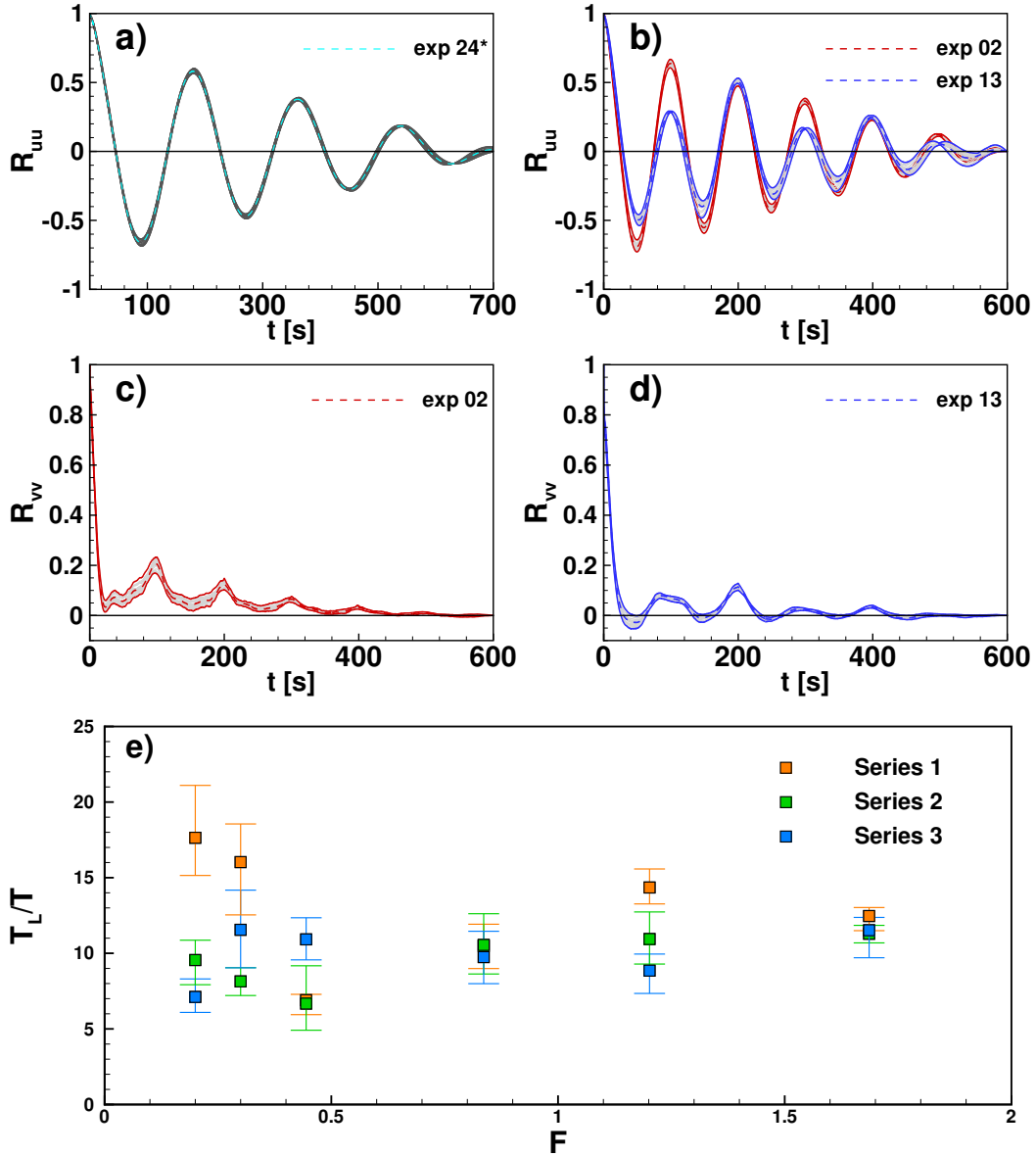


Figure 6. Autocorrelation functions. Panel a) R_{uu} experiment 24 of De Leo et al. Panel b) R_{uu} experiments 2 and 13. Panel c) R_{vv} experiment 2. Panel d) R_{vv} experiment 13. Panel e) non dimensional Lagrangian integral scales as a function of the form factor F . Squared symbols stand for averaged values whereas bars for their spreads.

347 we have performed a different Lagrangian analysis. In particular, we are interested to
 348 understand whether there is an influence of the initial conditions associated to particle
 349 release. A similar analysis has been discussed in Enrile et al. (2019), where single and
 350 multiple particle statistics have been computed starting from HF-radar total velocity fields
 351 of the Gulf of Trieste (Italy), a semi-enclosed coastal basin strongly dominated by tides.
 352 When Lagrangian analysis of the kind presented here are performed, the definition of
 353 the initial time for particle release is set to coincide with the starting time of the avail-
 354 able Eulerian field, which is formally correct when a statistically steady forcing gener-
 355 ates the Eulerian flow. We assumed that also for simple monochromatic forcing, exper-

356 iments of Part 1, the evaluation of the velocity autocorrelations and the integral scales
 357 were independent on the initial time of release. On the contrary, for the present exper-
 358 iments we have performed a sequence of Lagrangian computations, releasing the numer-
 359 ical particles at different times during a single wave period (semi-diurnal plus diurnal
 360 tidal signals) and, then, we have computed our target functions (\mathcal{R}_{uu} , \mathcal{R}_{vv} and the cor-
 361 responding integral scales) averaging them. In particular, we repeated the computation
 362 using 20 initial times, each one separated by a lag equal to $T_d/20$, being T_d the period
 363 of the diurnal constituent, which is the period of the wave packet. The results of this pro-
 364 cedure are shown in Figures 6a) - d). Grey lines indicate the output of the single run,
 365 whereas thick solid lines the lower and higher envelope and the thick dashed line the av-
 366 erage functions. Panel a) shows the longitudinal velocity autocorrelation function \mathcal{R}_{uu}
 367 for the case of experiment 24, monochromatic tidal case of Part 1, for comparison. As
 368 expected there is no influence of the initial conditions of the particle release, all func-
 369 tions are substantially coincident. Panels b), c) and d) show the autocorrelation func-
 370 tions for two experiments, namely experiment 2 (red lines) and 13 (blue lines). The lon-
 371 gitudinal velocity autocorrelations (see Figure 6b) show a dependence on the initial con-
 372 ditions only for the values of \mathcal{R}_{uu} , without visible modifications of the periodicity of the
 373 oscillations. As in the case of the monochromatic tidal waves, the longitudinal autocor-
 374 relations have intense negative lobes, which influence the dispersion regimes for time of
 375 same order of the Lagrangian time scale. The behavior of the spanwise autocorrelation
 376 function \mathcal{R}_{vv} , panel c) and d) is more interesting. The subsequent releases produce a wider
 377 spread of the autocorrelations values and, more importantly, the negative lobes are likely
 378 to appear for particular initial times. It is not simple to relate the different autocorre-
 379 lation function shapes with the initial times and not particularly relevant: the main point
 380 is that particles tend to decorrelate themselves from their initial conditions differently
 381 if released at different instants during a multiple constituents tidal period. Moreover, the
 382 presence of negative lobes will impact on the computation of the Lagrangian time scales,
 383 being the latter the integral of the autocorrelation functions. The resulting Lagrangian
 384 integral scales are shown in Figure 6e). The symbols represent the average values of T_L ,
 385 whereas the bars indicate the spread of the computed values that reach also a consid-
 386 erable percentage of the mean decorrelation time. The Lagrangian scales computed for
 387 all the different releases oscillate around a mean value with a periodicity similar to the
 388 semi-diurnal period (data not shown), with a behavior similar to the one described in
 389 Enrile et al. (2019). As in the case of monochromatic tides, T_L remains always much shorter
 390 than the tidal period.

391 5.2 Absolute dispersion regimes and its dependence on the tidal shape

392 In the previous section, we have shown how the complex forcing requires a partic-
 393 ular attention in the analysis of the decorrelation time scales and how the initial time
 394 of the particle release ultimately leads to different autocorrelation functions. We are now
 395 interested to analyze the effect on the average dispersion processes in terms of single par-
 396 ticle statistics. In fact, starting from the numerical trajectories of particle tracers released
 397 uniformly on the domain, we computed the diagonal components of the absolute disper-
 398 sion tensor as

$$399 \quad A_{ii}^2(t, t_0) = \left\langle |x_i(t) - x_i(t_0)|^2 \right\rangle = \frac{1}{N} \sum_{i=1}^N |x_i(t) - x_i(t_0)|^2, \quad (4)$$

400 where the brackets indicate average over the particle ensemble, $x_i(t)$ is the posi-
 401 tion of the i -th particle at time t that started in position $x_i(t_0)$ at t_0 , and N is the to-
 402 tal number of particles in the ensemble. We then define the total absolute dispersion $a^2(t)$
 403 as the trace of the absolute defined by equation (4) (Elhmaïdi et al., 1993; Provenzale,
 404 1999). The time derivative of $a^2(t)$ is related to the total dispersion coefficient K . It is
 405 well known that depending on the time behavior of the total absolute dispersion, $a^2 \propto$
 406 t^α , different dispersion regimes can be distinguished. A *diffusive* (or *Brownian*) regime

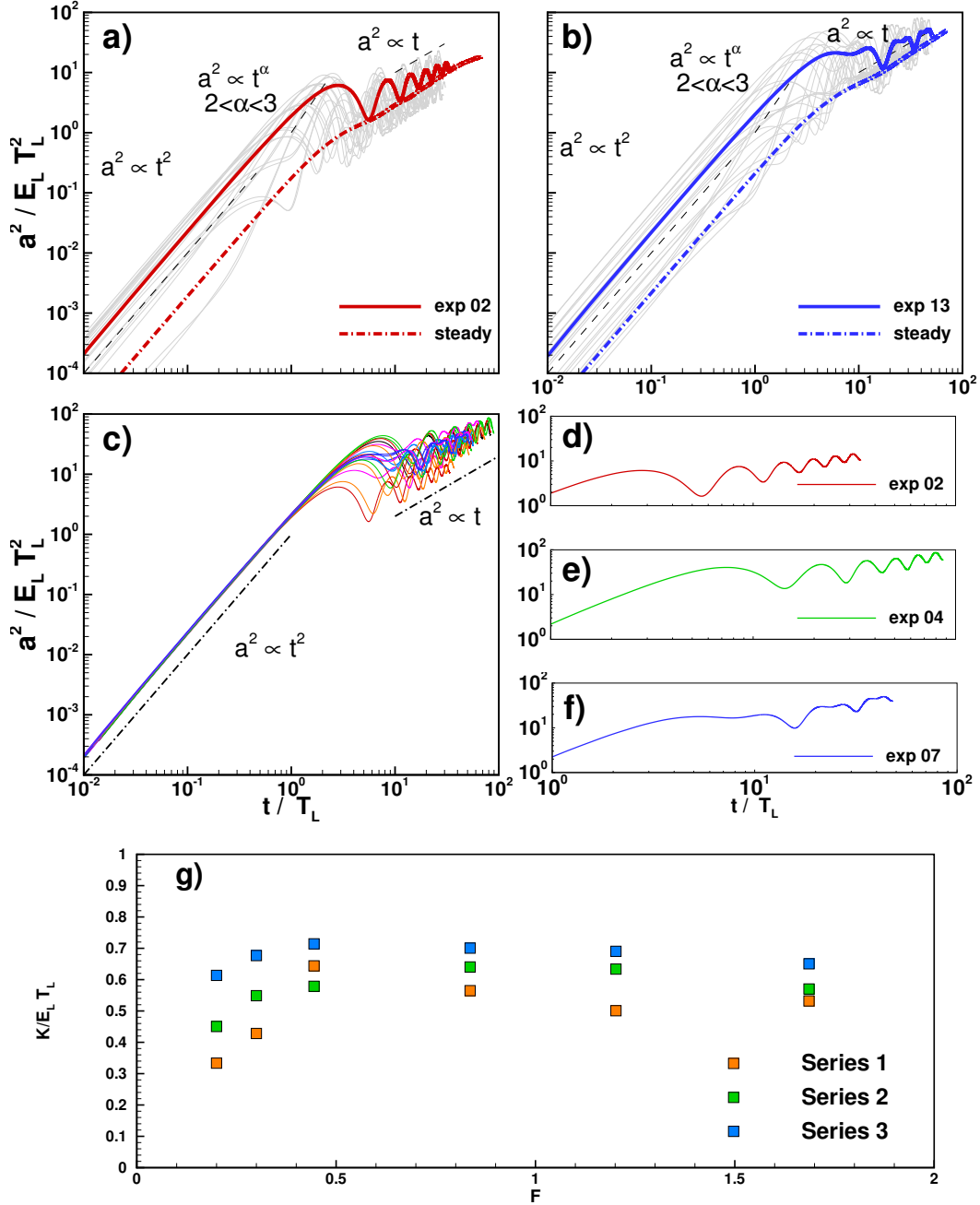


Figure 7. Example of the results obtained from single particle statistics analysis. a) Non dimensional total absolute dispersion as a function of the non dimensional time for experiment 2, b) and experiment 13: grey lines refer to different initial particles releasing, red solid lines to their averaged, red dash-dotted lines indicate the total absolute dispersion inferred from the residual current flow. Regimes are plotted in black dashed lines. c) Averaged total absolute dispersion for all experiments. Focus on linear regimes: d) experiment 2, e) experiment 4 and f) experiment 7. g) Estimated values of the dimensionless diffusion coefficient $K / (E_L T_L)$ as a function of the form factor F .

407 is found for $\alpha = 1$ and it is associated to a constant diffusion coefficient K (Taylor, 1921).
 408 Super (sub)- diffusive regimes are related to exponents greater (smaller) than 1. Sub-
 409 diffusive regimes are observed when the velocity autocorrelation functions show a first
 410 negative lobe, whose integral is greater than the first positive lobe (Berloff et al., 2002;
 411 Veneziani et al., 2004). Looping like correlations are observed in several oceanographic
 412 contexts and may be produced by meso-scale vortical structures (Berloff et al., 2002; Veneziani
 413 et al., 2004; LaCasce, 2008) or when a periodic forcing as a tide plays an important role
 414 (Enrile et al., 2019). Moreover, sub-diffusive regime can be generated by domain char-
 415 acteristics where the flow is generated. In particular, semi-enclosed domain could im-
 416 pose an upper limit for the maximum displacement of the tracer particles respect to their
 417 initial position (Artale et al., 1997). On the contrary, a pronounced first positive lobe
 418 is usually associated to super-diffusive regime with an exponent α in a range between
 419 2 and 3 (Veneziani et al., 2004), being $\alpha = 2$ the initial ballistic regime for time less
 420 than T_L .

421 A single constituent tidal forcing is able to generate looping like autocorrelation
 422 functions and, possibly, leading to super-diffusive regime that appears for time of the or-
 423 der of the Lagrangian integral scales. This regime is a transition between an initial bal-
 424 listic regime and the asymptotic diffusive regime $a^2 \propto t$, as we have described in the
 425 Part 1. In the present case of multiple-constituents, we have performed the calculation
 426 of the absolute dispersion using the same strategy as for the autocorrelation functions,
 427 i.e. using multiple particle deployment within the longest period (diurnal tide). Typi-
 428 cal results of the computation of the total absolute dispersion and the corresponding dif-
 429 fusive coefficients are shown in Figure 7. Note that the total absolute dispersion a^2 and
 430 the total diffusive coefficient K have been made dimensionless using the ensemble av-
 431 eraged Lagrangian kinetic energy per unit mass $E_L = 1/2\langle(u_L(\mathbf{x}, t)^2 + v_L(\mathbf{x}, t)^2)\rangle$ and
 432 the Lagrangian integral scale T_L , coherently with the monochromatic experiments. Pan-
 433 els a) and b) show the results of two typical experiments, namely experiment 2 and 13,
 434 for the dimensionless $a^2(t)/(E_L T_L^2)$ as a function of the dimensionless time t/T_L . Grey
 435 lines represent the output of the single deployment, whereas the solid red line the av-
 436 erage over the different releases of the total absolute dispersion. The effects of the ini-
 437 tial conditions are clearly visible and produce a bundle of curves that, however, tend to
 438 similar regimes for long times. This has been also observed by Enrile et al. (2019) where
 439 the spread of the different curves was calculated and a decrease in time was observed.
 440 Physically, this suggests that after several tidal cycles the particles are no longer influ-
 441 enced by their initial conditions. However, this further time scale of the process must
 442 not be confused with the Lagrangian integral scale T_L that separates the *ballistic* regime
 443 from the *Brownian* regime, when the latter exists. Interestingly, all total absolute dis-
 444 persion curves tend to a diffusive regime for $t/T_L \gtrsim 10$ regardless the initial conditions,
 445 which is well described by the averaged $a^2(t)/(E_L T_L^2)$ (red solid line). For $t/T_L \lesssim 1$ a
 446 *ballistic* regime is always recovered, whereas super-diffusive regime $a^2(t)/(E_L T_L^2) \propto t^{2\div 3}$
 447 appears only for some particle deployments and this is coherent with the autocorrela-
 448 tion functions that might show intense positive lobes after negative ones, see Figure 6.
 449 Moreover, panel a) and b) also report the non dimensional total dispersion evaluated us-
 450 ing the residual currents only (dash-dotted lines). As already shown for the single har-
 451 monic experiments, the residual currents lead to a time dependence of the total abso-
 452 lute dispersion that substantially filters out the oscillations due to the periodic veloc-
 453 ity fields, leaving unaltered the overall slope of the curves. This could demonstrate how
 454 the net particle dispersion is produced by the residual currents as claimed in tidal flows
 455 (MacCready, 1999; Valle-Levinson, 2010). The total non dimensional averaged disper-
 456 sion for all experiments are plotted in Figure 7 panel c). Averaging over a great num-
 457 ber of initial condition leads to hidden possible super-diffusive regimes and all curves to
 458 collapse onto a *ballistic* initial regime. However, we are interested in long time statistics
 459 as these describe the typical dispersive regimes that could occur in realistic conditions
 460 after many tidal cycles. All experiments shown in panel c) reach an asymptotic diffu-
 461 sive regime with some behaviors related to the shape of the tidal waves. In particular,

462 the oscillations observed for $t/T_L \gtrsim 10$ depend on the form factor F and show typical
 463 periods depending on its values, see Figure 4 panels d)-f) where three experiments are
 464 displayed. Experiments 2 and 4 are characterized by tidal waves dominated by the semi-
 465 diurnal components, $F = 0.2$ and $F = 0.44$, respectively, whereas experiment 7 cor-
 466 responds to a mixed tide mainly diurnal ($F = 1.668$). The observed oscillations are co-
 467 herent with the dominant frequency of the forcing tides.

468 Finally, we have evaluated the non dimensional total diffusion coefficient $K/(E_L T_L)$
 469 to understand the role of the tidal wave shape. As in the monochromatic case, the greater
 470 contribution to $K/(E_L T_L)$ is provided by the longitudinal dispersion, which accounts for
 471 more than 95% of its value. As noted in the companion paper and following Besio et al.
 472 (2012), it is important to understand which mixing processes are described by the cal-
 473 culated coefficients. In the present case, the residual current has been calculated by tak-
 474 ing the average over the tidal periods of the time dependent Eulerian velocity fields and
 475 no other decomposition have been performed (Valle-Levinson, 2010). This implies that
 476 our procedure yields to the estimate of a total diffusive coefficient ($K = K_x + K_y$) as
 477 the sum of a longitudinal coefficient (K_x) and a transverse coefficient (K_y). The latter
 478 coefficients include also the turbulent diffusion contribution. This is important when a
 479 comparison is attempted with other laboratory and/or field measurements (Fischer et
 480 al., 1979; Monismith et al., 2002; Lewis & Uncles, 2003; Banas et al., 2004). Figure 4 panel
 481 g) shows the estimated values of the dimensionless diffusion coefficient $K/(E_L T_L)$ as a
 482 function of the form factor F . The results suggest that mixed tides enhance the over-
 483 all longitudinal dispersion with respect to monochromatic tides. In fact, the values of
 484 the total non dimensional coefficient show a maximum around $F = 0.5$ and then a slow
 485 decrease for increasing F . A second interesting observation regards the effect of the phase
 486 lag between the tidal constituents. On average, phase lag $\phi = \pi/4$, namely a lag in the
 487 diurnal constituent, produces higher diffusion coefficients. The range of values of $K/(E_L T_L)$
 488 is in agreement with the values obtained for the monochromatic case. A direct compar-
 489 ison with field observations specifically performed to understand the role of the tidal wave
 490 shape is complicated by the fact that no information on the typical tides are reported
 491 in the studies (Monismith et al., 2002; Lewis & Uncles, 2003; Banas et al., 2004). Fol-
 492 lowing the scaling argument discussed in the companion paper, Part 1, we expect that
 493 the non dimensional values of the total diffusion coefficient fall in the observed ranges
 494 in real estuaries. However, it would be interesting to verify the tendency of a mixed tide
 495 to increase the longitudinal dispersion.

496 5.3 The interplay of flow structures at different scales.

497 The analysis of the Eulerian time dependent fields discussed in section 4 has shown
 498 that even in a relatively simple geometry, as the one used in the present experimental
 499 campaign, flow structures at different scales are generated and, more interestingly, they
 500 interact during a tidal cycle. The asymptotic dispersion regime has proven to exist as
 501 an average process over the entire domain. In this section, we are interested to discuss
 502 the interplay among the particle trajectories and the different scales of the flow. To this
 503 end we apply tools commonly reported as multiple particle statistics, see LaCasce (2008)
 504 for a review and application to geophysical contexts. Differently from the single parti-
 505 cle statistics of section 3, here we follow the separation of couple of particles in time, com-
 506 puting the relative dispersion. The relative dispersion matrix $\mathbf{R}^2(t)$ is defined as the mean-
 507 square distance at time t between a pair of particles that at time t_0 had a distance equal
 508 to r_0 :

$$509 \quad R_{ij}^2(t) = \frac{1}{M-1} \sum_{m=1}^{M-1} \{ [x_i^m(t) - x_i^{m+1}(t)] [x_j^m(t) - x_j^{m+1}(t)] \} \quad (5)$$

510 where $M-1$ is the number of particle pairs. As for the total absolute dispersion a^2 , the
 511 total relative dispersion $r^2(t)$ is simply the trace of the relative dispersion matrix $\mathbf{R}^2(t)$
 512 and the total relative diffusivity $K^{(2)}(t)$ is its time derivative. Together with the rela-

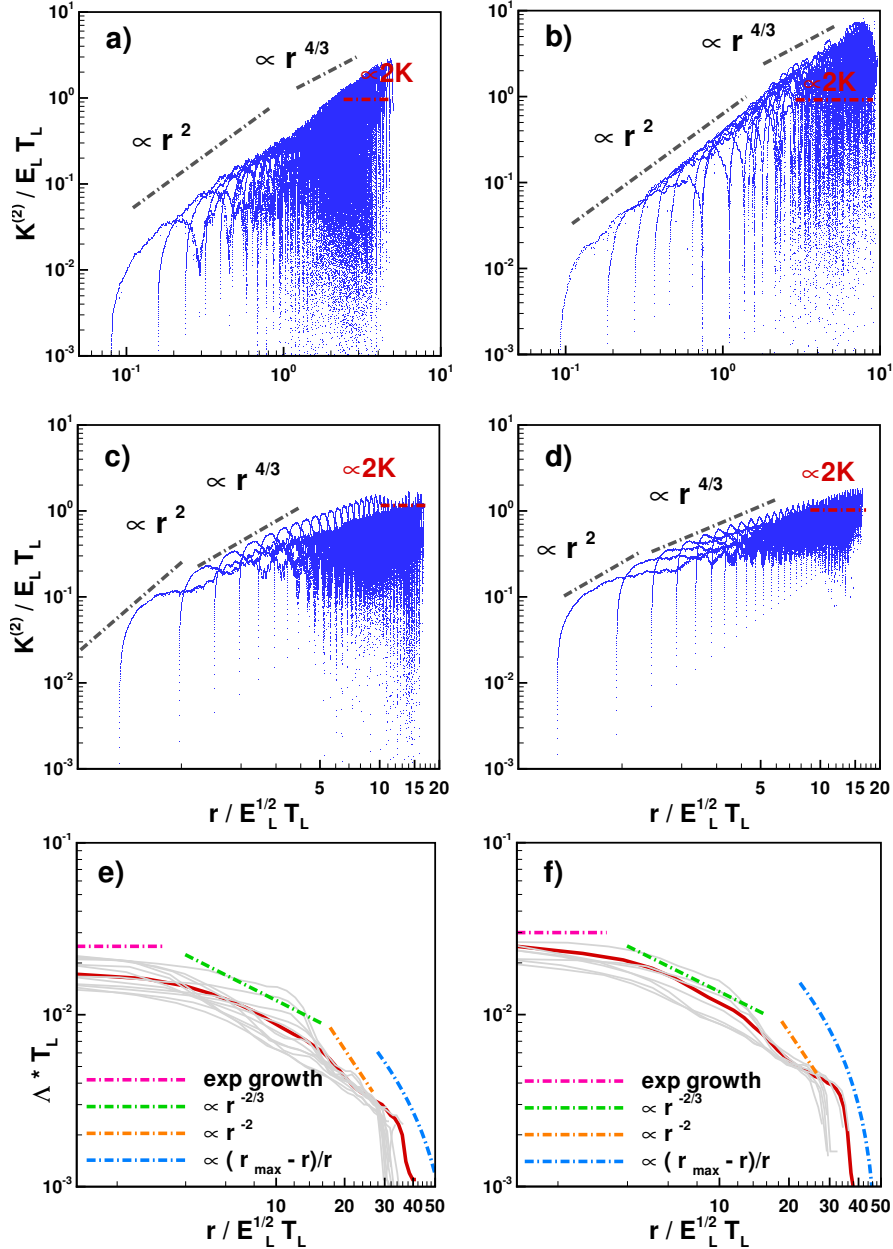


Figure 8. Example of the results obtained from multiple particle statistics analysis. a) dimensionless relative dispersion coefficient as a function of the non dimensional separation of the case of the monochromatic tide experiment number 18. b) same as panel a for the case of the monochromatic tide experiment number 26; c) same as panel a for the experiment 4 of series 1; d) same as panel a for the experiment 13 of series 1; e) non dimensional FSLE as a function of the non dimensional separation for experiment 4 of series 1; f) non dimensional FSLE as a function of the non dimensional separation for experiment 13 of series 1. In each panel the expected theoretical laws are also reported.

513 tive dispersion, we employ another Lagrangian measure commonly used in dispersion stud-
 514 ies, namely the Finite Scale Lyapunov Exponents Λ (FSLE). FSLE consists in average

515 the times required to a pair to separate from an initial distance to a final one (i.e. Ar-
 516 tale et al., 1997; LaCasce, 2008; Cencini & Vulpiani, 2013). Thus, in order to calculate
 517 the FSLE it is necessary to first choose a set of distances that are recursively increased
 518 as:

$$519 \quad r_n = \beta r_{n-1} = \delta^n r_0, \quad (6)$$

520 where n is the chosen number of separation and β is an arbitrary constant larger than
 521 unity, and then to calculate the times required (known as “exit time” T_n) for each pair
 522 displacement to grow to the successive r_n . At each distance the maximum FSLE is com-
 523 puted as:

$$524 \quad \Lambda(r) = \frac{1}{\log(\beta)} \left\langle \frac{1}{T_n} \right\rangle, \quad (7)$$

525 where the brackets indicate an ensemble average over the particle pairs that effectively
 526 reach the r_n distance. Care must be taken in the choice of the multiplier δ in order to
 527 correctly capture the regimes of the flow at hand (Haza et al., 2008). In our experiments,
 528 we set $\delta = 1.2$ as seen in Enrile et al. (2019). Both relative dispersion and FSLE have
 529 been extensively used in oceanographic and costal studies leading to a better compre-
 530 hension of the physical processes at the different separation scales (Artale et al., 1997;
 531 Orre et al., 2006; LaCasce, 2008; Haza et al., 2008; Enrile et al., 2018, 2019). The suc-
 532 cess of the use of the two measures in geophysical applications relies on classical stud-
 533 ies on 2D and atmospheric turbulence (Kraichnan, 1966; Lin, 1972; Er-El & Peskin, 1981;
 534 Bennett, 1984; Babiano et al., 1990). The main results were the existence of two distinct
 535 dynamical mechanisms leading to two dispersion regimes, namely *local dispersion* and
 536 *non-local dispersion* and the link between the scaling law of these regimes with the en-
 537 ergy cascade (inverse energy cascade and direct enstrophy cascade). Scaling arguments
 538 to describe the different dispersion and energy regimes can be summarized searching for
 539 laws of the kind: $K^{(2)} \propto r^{(\alpha+1)/2}$. The link with the energy cascades is the value of the
 540 exponent α , having assumed the turbulent energy spectrum as a function of the wave
 541 numbers in the form of $E(k) \propto k^{-\alpha}$. Relative dispersion in *local dynamics* is charac-
 542 terized by the effect of local straining, which is not efficient in producing large separa-
 543 tion, and the dispersion of pairs is dominated by eddies of the same scale of their sep-
 544 aration. This regime is described by values $1 < \alpha < 3$ and, in particular, for $\alpha = 5/3$
 545 the famous Richardson-Obukhov law is recovered with $K^{(2)} \propto r^{4/3}$, that corresponds
 546 to the energy cascade $E(k) \propto k^{-5/3}$. On the contrary, *non-local dynamics* is charac-
 547 terized by the effect of vortices with typical scale much larger than the separation. This
 548 regime is described by the Kraichnan-Lin law $K^{(2)} \propto r^2$, or more generally for $\alpha >$
 549 3 . In this case, the expected energy spectrum corresponds to an enstrophy cascade $E(k) \propto$
 550 k^{-3} . Note that where the relative dispersion shows a power law dependence, the FSLEs
 551 exhibit a power law dependence on the separation as $\Lambda \propto r^{-2/\gamma}$. The exponent γ is linked
 552 to the time growth of r^2 with time (LaCasce, 2008).

553 The computation of $r^2(t)$, $K^{(2)}$ and $\Lambda(r)$ has been performed on both data sets,
 554 single and multiple constituents tides, with the aim to understand which are the typi-
 555 cal regimes and if different regimes are triggered by more complex forcing. In the case
 556 of multiple constituents we again performed a series of simulations varying the initial time
 557 of deployment. Figure 8 shows the typical results for the relative dispersion, the dimen-
 558 sionless relative diffusivity coefficient $K^{(2)}/(E_L T_L)$ as a function of the dimensionless sep-
 559 arations $r/(E_L^{1/2} T_L)$, for experiments forced by a single harmonic tide, panel a) and b)
 560 (experiment 18 and experiment 26) and for experiments 4 and 13 of the present labo-
 561 ratory campaign, panel c) and d). In the same plots the theoretical laws, namely the Richardson-
 562 Obukhov law and the Kraichnan-Lin law, are shown to help the identification of the regimes.
 563 It is interesting to note that in all cases, regardless the characteristics of the tidal wave,
 564 two distinct regimes can be observed. For separation smaller than a typical injection scale
 565 $r_i/(E_L^{1/2} T_L)$, the diffusivity coefficient grows as $K^{(2)}/(E_L T_L) \propto (r/(E_L^{1/2} T_L))^2$, whereas
 566 for separation larger than the injection scale the regime follows closely the Richardson-
 567 Obukhov law. Correctly for very large separation the growth of the relative diffusivity

568 coefficient attains a constant value $K^{(2)}/(E_L T_L) \approx 2K/(E_L T_L)$, where $K/(E_L T_L)$ is
 569 the total absolute diffusivity coefficient discussed in the previous section. The injection
 570 scale $r_i/(E_L^{1/2} T_L)$ is very close to the Lagrangian integral spatial scale. In fact, the change
 571 in the relative dispersion regime is close to $r/(E_L^{1/2} T_L) \approx 1$. The two-regime scenario
 572 is also confirmed by the trends of the dimensionless FSLE ΔT_L as a function of the di-
 573 mensionless separation ($r/(E_L^{1/2} T_L)$), see panel e) and f). As for the autocorrelation func-
 574 tions, grey lines indicate the output for the different deployments, whereas the solid lines
 575 represent the averaged value. Also in this case we have reported the expected theoret-
 576 ical laws (Artale et al., 1997). The Kraichnan-Lin law previously described is found for
 577 $r/(E_L^{1/2} T_L) < r_i/(E_L^{1/2} T_L)$ and implies an exponential growth of the FSLEs. As the
 578 separation r increases, the FSLE slope suggests the presence of both the Richardson-Obukhov
 579 regime $\Delta T_L \propto (r/(E_L^{1/2} T_L))^{-2/3}$ and the linear regime $\Delta T_L \propto (r/(E_L^{1/2} T_L))^{-2}$. More-
 580 over, the FSLE for very large separation exhibits the limiting regime expected for sep-
 581 aration close to the saturation length r_{max} , i.e. the maximum separation imposed by the
 582 domain. This is typical for semi-enclosed basins as observed in similar geometrical con-
 583 texts (Artale et al., 1997; Cencini & Vulpiani, 2013; Enrile et al., 2019).

584 Therefore, the results suggest that *local dispersion* is the dominant process for most
 585 of the separation range and, from a physical standpoint, this could be explained by the
 586 presence of large scale macro-vortices as the dominant features in all tidal cases so that
 587 separations are influenced by local straining produced by the mentioned macrovortices.
 588 Moreover, the overall picture seems not to be influenced by tidal wave shape and phase
 589 lag between the constituents and this could be explained observing that all the cases are
 590 able to trigger similar macro-vortices. Note that the computation of the multiple par-
 591 ticle statistics, similarly to the single particle statistics, is averaged over the ensemble
 592 of particles deployed uniformly over the domain. This standard procedure relies on the
 593 assumption of homogeneity of the flow under investigation (Berloff et al., 2002). Thus,
 594 the observed regimes must be considered as the average behavior of the Lagrangian dis-
 595 persion.

596 Finally, it is worth noting that the injection separation r_i has been described as
 597 of the same order of magnitude of the Lagrangian integral length scale. However, another
 598 length scale could play a role in the present experiments, namely the length of the side
 599 wall of the tidal inlet l_i . As previously noted, the generation of the flood-macro-vortices
 600 is controlled by the vortex shedding from the corners of the tidal inlet. This mechanism
 601 could be also explained in analogy with the vortex generation downstream a coastal head-
 602 land, where the extent of the headland is a controlling length scale of the process (Signell
 603 & Geyer, 1991; Davies et al., 1995). Two observations might be important for the present
 604 case. Firstly, the l_i is very close to the Lagrangian integral spatial scale. Secondly, the
 605 flow could be described as a forced turbulence, where the forcing is the presence of the
 606 tidal inlet and, thus, l_i could be regarded as the length scale of the injected energy. We
 607 clearly observed a vortex merging process that several times is a signature of an inverse
 608 energy cascade process. A further piece of information that could confirm this scenario
 609 is the presence of two distinct regimes in the relative dispersion and in the FSLE, sep-
 610 arated by the injection scale r_i . However, further analyses are required to provide a sound
 611 proof of the existence of an inverse energy cascade, which would require the evaluation
 612 of the energy spectrum and higher order structure functions (Nikora et al., 2007; Alex-
 613 akis & Biferale, 2018; Enrile et al., 2020).

614 6 Conclusions

615 In the present study, we have reported the main results obtained from an Eulerian
 616 and Lagrangian analysis of an extensive laboratory campaign on the dispersion processes
 617 generated by tidal waves composed by multiple harmonics. The two dimensional veloc-
 618 ity fields measured in a large scale physical model allowed for an analysis of the flow struc-
 619 tures generated by complex tidal waves in a geometry that mimics a weakly convergent

and weakly dissipative estuary (Toffolon et al., 2006) open to the sea through a barrier-island type inlet (Nicolau del Roure et al., 2009). It has been observed that the tidal wave shape, represented by the form factor F , and the constituent phase lag strongly influence the generation of the flood-macrovortices in terms of typical length scales. We confirm that the presence of the tidal flats induces the ebb-dominance regardless the typical Strouhal number confirming field observation and in apparent contrast with previous laboratory observation (Wells & van Heijst, 2004; Nicolau del Roure et al., 2009). It is worth noting that a vortex merging mechanism at the tidal inlet has been observed also in the present case as for the single harmonic experiments. Moreover, the residual current seems to be less sensitive to the tidal wave shapes, being very similar to the one generated by a single harmonic tide, as presented in the companion paper. Regarding the Lagrangian properties of the flow, the shape of the tidal waves plays a significant role on the resulting autocorrelation velocity functions as pointed out by the analysis performed varying the initial release time of the particles. On average the total absolute dispersion reached in all cases an asymptotic diffusive regime and the corresponding total diffusivity coefficients K showed a non monotonic trend with the form factor. Mixed tides, mainly semi-diurnal, seem to be more efficient for a longitudinal dispersion. Regarding the multiple particle dispersion processes, both the regimes in the total relative diffusion coefficient and the FSLEs show that the flow is dominated by two regimes for separations lower or greater of a typical injection scale, which seems to be equal to the Lagrangian integral length scale of the lateral extension of the tidal inlet. The Richardson regime of *local dynamics* dominates for a wide range of separation larger than r_i and smaller of a saturation length highlighted in the FSLE trends. Tidal flows are governed by large macro-vortices larger than the mean separation.

The present experiments together with the results discussed in the companion paper, dedicated to the single harmonic tide, have provided a deep understanding of the main dispersion processes occurring in weakly-dissipative estuaries. Two main aspects will require dedicated studies and will be the directions for future insights. Firstly, the role of the flow inhomogeneities that have been hidden so far by the use of Lagrangian statistics based on homogeneous measures (single and multiple particle statistics). Tidal flows have been proved to be able to generate chaotic mixing leading to more complex behaviors (Zimmerman, 1986; Ridderinkhof & Zimmerman, 1992; Orre et al., 2006) that could be interpreted in terms of Lagrangian Coherent Structures (Haller, 2015). Finally, a new dedicated series of experiments, with higher spatial and temporal resolution, will be planned to find an answer to the question whether or not an inverse energy cascade occurs in this class of flows. The possible presence of an inverse energy cascade is quite important also for defining a correct approach in numerical modeling of these important geophysical flows.

Acknowledgments

This research has not been supported by external funding. The Authors declare no conflict of interests. All results are based on large scale PIV measurements, owing to the excessive dimensions of the data set no web repository has been prepared. Data Management Repository available at doi: <https://doi.org/10.5281/zenodo.5006407>.

References

- Alexakis, A., & Biferale, L. (2018). Cascades and transitions in turbulent flows. *Physics Reports*, *767*, 1–101.
- Amin, M. (1986). On the conditions for classification of tides. *The International Hydrographic Review*.
- Artale, V., Boffetta, G., Celani, A., Cencini, M., & Vulpiani, A. (1997). Dispersion of passive tracers in closed basins: Beyond the diffusion coefficient. *Physics of Fluids*, *9*(11), 3162–3171.

- 671 Babiano, A., Basdevant, C., Le Roy, P., & Sadourny, R. (1990). Relative dispersion
672 in two-dimensional turbulence. *J. Fluid Mech.*, *214*, 535-557.
- 673 Banas, N., Hickey, B., MacCready, P., & Newton, J. (2004). Dynamics of willapa
674 bay, washington: A highly unsteady, partially mixed estuary. *Journal of Physi-
675 cal Oceanography*, *34*(11), 2413-2427.
- 676 Bennett, A. (1984). Relative dispersion: Local and nonlocal dynamics. *J. Atm Sc.*,
677 *41*, 1881-1886.
- 678 Berloff, P. S., McWilliams, J. C., & Bracco, A. (2002). Material transport in oceanic
679 gyres. part i: Phenomenology. *Journal of Physical Oceanography*, *32*(3), 764-
680 796.
- 681 Besio, G., Stocchino, A., Angiolani, S., & Brocchini, M. (2012). Transversal and lon-
682 gitudinal mixing in compound channels. *Water Resources Research*, *48*(12).
- 683 Cai, H., Savenije, H. H., & Toffolon, M. (2012). A new analytical framework for
684 assessing the effect of sea-level rise and dredging on tidal damping in estuaries.
685 *Journal of Geophysical Research: Oceans*, *117*(C9).
- 686 Cencini, M., & Vulpiani, A. (2013). Finite size lyapunov exponent: review on appli-
687 cations. *Journal of Physics A: Mathematical and Theoretical*, *46*(25), 254019.
- 688 Cucco, A., Umgiesser, G., Ferrarin, C., Perilli, A., Canu, D. M., & Solidoro, C.
689 (2009). Eulerian and lagrangian transport time scales of a tidal active coastal
690 basin. *Ecological Modelling*, *220*(7), 913-922.
- 691 Davies, P. A., Dakin, J. M., & Falconer, R. A. (1995). Eddy formation behind a
692 coastal headland. *Journal of Coastal Research*, 154-167.
- 693 Elhmaïdi, D., Provenzale, A., & Babiano, A. (1993). Elementary topology of
694 two-dimensional turbulence from a lagrangian viewpoint and single-particle
695 dispersion. *Journal of Fluid Mechanics*, *257*, 533-558.
- 696 Enrile, F., Besio, G., & Stocchino, A. (2020). Eulerian spectrum of finite-time ly-
697apunov exponents in compound channels. *Meccanica*, *55*(9), 1821-1828.
- 698 Enrile, F., Besio, G., Stocchino, A., Magaldi, M., Mantovani, C., Cosoli, S., . . .
699 Poulain, P. (2018). Evaluation of surface lagrangian transport barriers in the
700 gulf of trieste. *Continental Shelf Research*, *167*, 125-138.
- 701 Enrile, F., Besio, G., Stocchino, A., & Magaldi, M. G. (2019). Influence of initial
702 conditions on absolute and relative dispersion in semi-enclosed basins. *Plos
703 one*, *14*(7), e0217073.
- 704 Er-El, J., & Peskin, R. (1981). Relative diffusion of constant-level balloons in the
705 suthern hemisphere. *J. Atm Sc.*, *38*, 2264-2274.
- 706 Fagherazzi, S., Wiberg, P. L., Temmerman, S., Struyf, E., Zhao, Y., & Raymond,
707 P. A. (2013). Fluxes of water, sediments, and biogeochemical compounds in
708 salt marshes. *Ecological Processes*, *2*(1), 1-16.
- 709 Fischer, H. B., List, J. E., Koh, C. R., Imberger, J., & Brooks, N. H. (1979). *Mixing
710 in inland and coastal waters*. Academic press.
- 711 Fortunato, A. B., & Oliveira, A. (2005). Influence of intertidal flats on tidal asym-
712 metry. *Journal of Coastal Research*, *21*(5 (215)), 1062-1067.
- 713 Gisen, J. I. A., & Savenije, H. H. (2015). Estimating bankfull discharge and depth in
714 ungauged estuaries. *Water Resources Research*, *51*(4), 2298-2316.
- 715 Haller, G. (2015). Lagrangian coherent structures. *Annual Review of Fluid Mechan-
716 ics*, *47*, 137-162.
- 717 Haza, A. C., Poje, A. C., Özgökmen, T. M., & Martin, P. (2008). Relative disper-
718 sion from a high-resolution coastal model of the adriatic sea. *Ocean Modelling*,
719 *22*(1-2), 48-65.
- 720 Jay, D. A. (1991). Green's law revisited: Tidal long-wave propagation in channels
721 with strong topography. *Journal of Geophysical Research: Oceans*, *96*(C11),
722 20585-20598.
- 723 Kang, J., & Jun, K. (2003). Flood and ebb dominance in estuaries in korea. *Estuar-
724 ine, Coastal and Shelf Science*, *56*(1), 187-196.

- 725 Kraichnan, H. (1966). Dispersion of particle pairs in homogeneous turbulence. *Phys.*
726 *Fluids*, *9*, 1937-1943.
- 727 LaCasce, J. (2008). Statistics from lagrangian observations. *Progress in Oceanogra-*
728 *phy*, *77*, 1-29.
- 729 Lanzoni, S., & Seminara, G. (1998). On tide propagation in convergent estuaries.
730 *Journal of Geophysical Research: Oceans*, *103*(C13), 30793-30812.
- 731 Lee, S.-H., & Chang, Y.-S. (2019). Classification of the global tidal types based on
732 auto-correlation analysis. *Ocean Science Journal*, *54*(2), 279-286.
- 733 Lewis, R. E., & Uncles, R. J. (2003). Factors affecting longitudinal dispersion in es-
734 tuaries of different scale. *Ocean Dynamics*, *53*(3), 197-207.
- 735 Lin, J. (1972). Relative dispersion in the enstrophy cascading inertial range of homo-
736 geneous two dimensional turbulence. *J. Atmos. Sci.*, *29*, 394-396.
- 737 MacCready, P. (1999). Estuarine adjustment to changes in river flow and tidal mix-
738 ing. *Journal of Physical Oceanography*, *29*(4), 708-726.
- 739 Monismith, S. G., Kimmerer, W., Burau, J. R., & Stacey, M. T. (2002). Struc-
740 ture and flow-induced variability of the subtidal salinity field in northern san
741 francisco bay. *Journal of physical Oceanography*, *32*(11), 3003-3019.
- 742 Nicolau del Roure, F., Socolofsky, S. A., & Chang, K.-A. (2009). Structure and
743 evolution of tidal starting jet vortices at idealized barotropic inlets. *Journal of*
744 *Geophysical Research: Oceans*, *114*(C5).
- 745 Nikora, V., Nokes, R., Veale, W., Davidson, M., & Jirka, G. (2007). Large-scale tur-
746 bulent structure of uniform shallow free-surface flows. *Environ Fluid Mech.*, *7*,
747 159-172.
- 748 Okubo, A. (1970). Horizontal dispersion of floatable particles in the vicinity of veloc-
749 ity singularities such as convergences. In *Deep sea research and oceanographic*
750 *abstracts* (Vol. 17, pp. 445-454).
- 751 Orre, S., Gjevik, B., & LaCasce, J. H. (2006). Characterizing chaotic dispersion in a
752 coastal tidal model. *Continental Shelf Research*, *26*(12-13), 1360-1374.
- 753 Provenzale, A. (1999). Transport by coherent barotropic vortices. *Ann. Rev. Fluid*
754 *Mech.*, *31*, 55-93.
- 755 Ridderinkhof, H., & Zimmerman, J. (1992). Chaotic stirring in a tidal system. *Sci-*
756 *ence*, *258*(5085), 1107-1111.
- 757 Seminara, G., Lanzoni, S., Tambroni, N., & Toffolon, M. (2010). How long are tidal
758 channels? *Journal of Fluid Mechanics*, *643*, 479.
- 759 Signell, R. P., & Geyer, W. R. (1991). Transient eddy formation around headlands.
760 *Journal of Geophysical Research: Oceans*, *96*(C2), 2561-2575.
- 761 Taylor, G. (1921). Diffusion by continuous movement. *Proc. Lond. Math. Soc.*, *20*,
762 196-212.
- 763 Toffolon, M., Vignoli, G., & Tubino, M. (2006). Relevant parameters and finite am-
764 plitude effects in estuarine hydrodynamics. *Journal of Geophysical Research:*
765 *Oceans*, *111*(C10).
- 766 Tsimplis, M., Proctor, R., & Flather, R. (1995). A two-dimensional tidal model
767 for the mediterranean sea. *Journal of Geophysical Research: Oceans*, *100*(C8),
768 16223-16239.
- 769 Umgiesser, G., Ferrarin, C., Cucco, A., De Pascalis, F., Bellafore, D., Ghezzi, M.,
770 & Bajo, M. (2014). Comparative hydrodynamics of 10 mediterranean lagoons
771 by means of numerical modeling. *Journal of Geophysical Research: Oceans*,
772 *119*(4), 2212-2226.
- 773 Valle-Levinson, A. (2010). *Contemporary issues in estuarine physics*. Cambridge
774 University Press.
- 775 Veneziani, M., Griffa, A., Reynolds, A. M., & Mariano, A. J. (2004). Oceanic turbu-
776 lence and stochastic models from subsurface lagrangian data for the northwest
777 atlantic ocean. *Journal of physical oceanography*, *34*(8), 1884-1906.
- 778 Viero, D. P., & Defina, A. (2016). Water age, exposure time, and local flushing time
779 in semi-enclosed, tidal basins with negligible freshwater inflow. *Journal of Ma-*

- 780 *rine Systems*, 156, 16–29.
- 781 Vouriot, C. V., Angeloudis, A., Kramer, S. C., & Piggott, M. D. (2019). Fate of
782 large-scale vortices in idealized tidal lagoons. *Environmental Fluid Mechanics*,
783 19(2), 329–348.
- 784 Weiss, J. (1991). The dynamics of enstrophy transfer in two-dimensional hydrody-
785 namics. *Physica D*, 48, 272–294.
- 786 Wells, M., & van Heijst, G. (2004). Dipole formation by tidal flow in a channel.
787 In *International symposium on shallow flows. balkema publishers, delft* (pp.
788 63–70).
- 789 Zhang, Z., & Savenije, H. H. (2017). The physics behind van der burgh’s empirical
790 equation, providing a new predictive equation for salinity intrusion in estuar-
791 ies. *Hydrology and Earth System Sciences*, 21(7), 3287–3305.
- 792 Zimmerman, J. (1986). The tidal whirlpool: a review of horizontal dispersion by
793 tidal and residual currents. *Netherlands Journal of Sea Research*, 20(2-3), 133–
794 154.